analytical chemistry

pubs.acs.org/ac Article

Metal-Mediated Polydopamine Nanoparticles–DNA Nanomachine Coupling Electrochemical Conversion of Metal–Organic Frameworks for Ultrasensitive MicroRNA Sensing

Ting Bao, Ruobing Fu, Yuying Jiang, Wei Wen, Xiuhua Zhang, and Shengfu Wang*

Cite This: *Anal. Chem.* 2021, 93, 13475–13484 Read Online

ACCESS | Metrics & More | Article Recommendations | Supporting Information

ABSTRACT: The development of a robust sensing platform with an efficient probe assembly, and ingenious signal conversion is of great significance for bioanalytical application. In this work, a multipedal polydopamine nanoparticles–DNA (PDANs-DNA) nanomachine coupling electrochemical-driven metal–organic frameworks (MOFs) conversion-enabled biosensing platform was constructed. The PDANs-DNA nanomachine was designed based on Ca^{2+}-mediated DNA adsorption and target-triggered catalytic hairpin assembly on PDANs, which not only maintained the DNA immobilization simplicity but also possessed a high walking efficiency. PDANs-DNA nanomachine could walk fast on the electrode via multiple legs under exonuclease III driving, resulting in the formation of DNA dendrimers through two hairpins assembly. The MOFs (Fe-MIL-88-NH_2) probe was decorated on the DNA dendrimers to act as a porous metal precursor and converted into electroactive Prussian Blue by a controlled electrochemical approach, which was a facile, simple, and room-temperature approach compared with the commonly employed MOFs conversion methods. Using microRNA-21 (miRNA-21) as the model target, the proposed biosensor achieved miRNA-21 detection ranging from 10 aM to 10 pM with the detection limit of 5.8 aM. The proposed strategy presented a highly efficient walking platform with the ingenious electrochemical conversion of MOFs, providing more options for the design of an electrochemical platform and holding potential applications in clinical analysis and disease diagnosis.

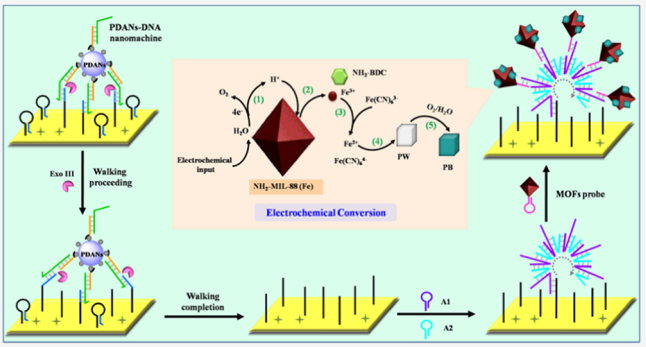

DNA nanomachines are artificial molecular machines with the features of flexible DNA assembly, diverse nanostructure, and controlled movement, which have become powerful tools in the biosensing field.[1−3] Based on the rational programming of DNA strands, a series of DNA nanomachines including DNA walker, DNA tweezers, and DNA motor have been designed.[4−6] Although these smart DNA nanomachines can perform different tasks along the designed track, the walking efficiency is still limited by the restricted DNA legs, which further affect the sensitivity of the system. To solve these problems, nanomaterials including gold nanoparticles and magnetic beads have been introduced to increase the loading capacity of walking tracks and DNA legs, whereas the immobilization process is mostly covalent probe conjugation and involved in the labeling of signal molecules, which is time-consuming and costly.[7−9] Therefore, the design of DNA nanomachines that maintain the DNA immobilization simplicity with a high walking efficiency and amplified signal output is of great significance.

Metal coordination plays an important role in building materials, which hold broad application prospects.[10] Polydopamine nanoparticles (PDANs), generated by the autoxidation of dopamine (DA), have attracted increasing attention in drug delivery, cancer therapy, biosensing, and bioimaging field with the advantages of easy synthesis, high coordination ability, and good biocompatibility.[11−13] As to the biosensing platform, PDANs are widely used as a substrate for DNA assembly through $\pi-\pi$ stacking interactions.[14,15] However, this adsorption pattern is susceptible to the competition of other biomolecules, which affects the performance of the biosensor. The catechol groups of PDANs are ideal metal ligands, so metal coordination is a simple and effective approach for PDAN functionalization, in which the surface catechol groups first coordinate with metal ions and then the adenosines of DNA interact with metal ions to induce DNA bridge on PDANs. Therefore, PDANs can act as useful nanocarriers of DNA (PDANs-DNA) based on the metal-mediated DNA

Received: May 20, 2021
Accepted: September 20, 2021
Published: September 29, 2021

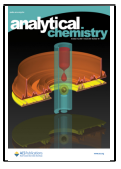

Scheme 1. Schematic Illustration of the Biosensor of miRNA-21 Based on PDANs-DNA Nanomachine and Electrochemical Conversion of MOFs: (A) Formation of Multipedal PDANs-DNA Nanomachine; (B) Fabrication Process of the Biosensor; and (C) Electrochemical Conversion of the MOFs Decorated on DNA Dendrimers

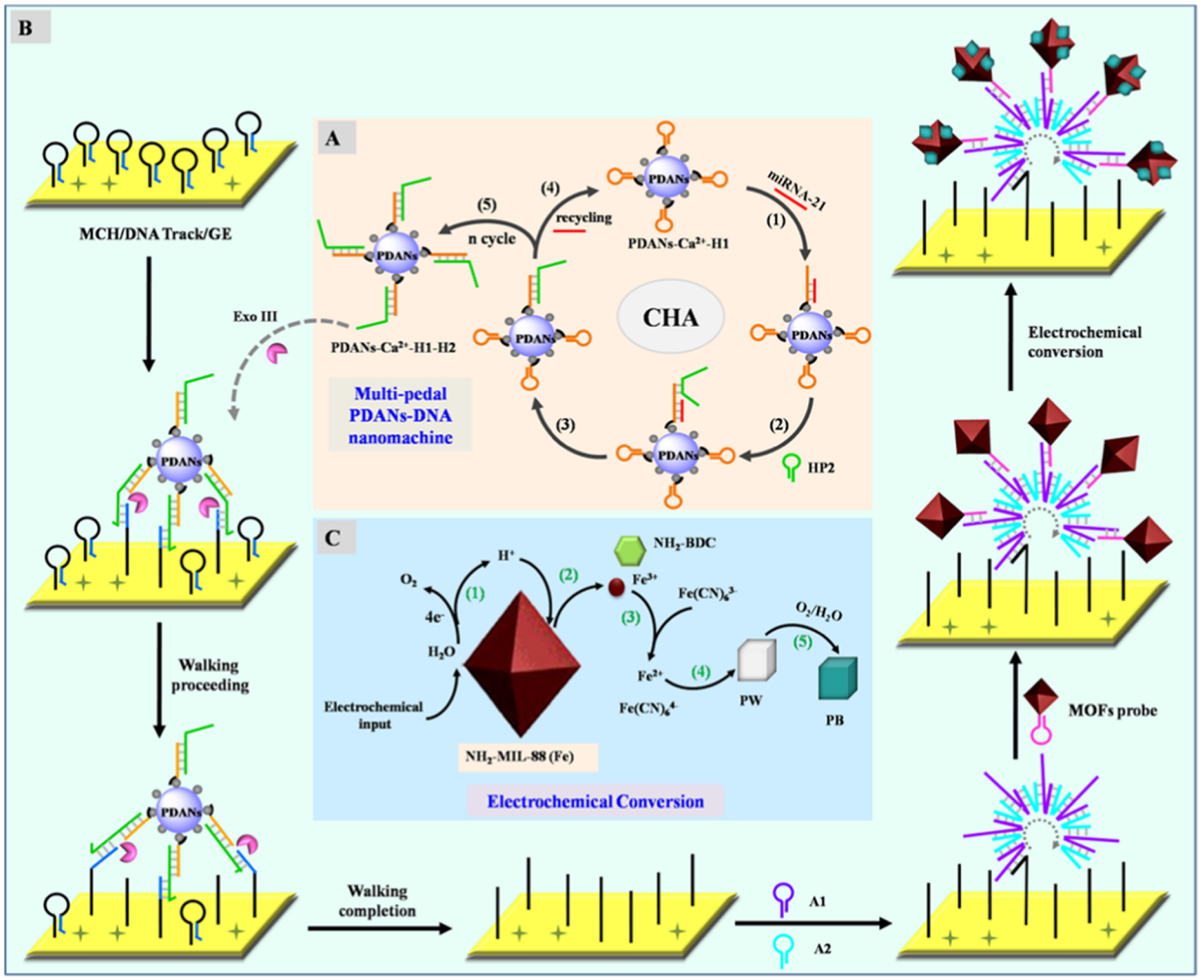

adsorption.[16,17] Compared with the traditional DNA assembly pattern, the metal-mediated PDANs-DNA possesses the advantages of fast assembly, high loading capacity, and high efficiency, which broaden the potential application of PDANs in the biosensing field.

Metal−organic frameworks (MOFs), assembled by metal cations and organic ligands, have become a rapidly developing field featuring high surface area, designable frameworks, well-defined pores, and easy modification.[18,19] The exploitation of various fascinating nanomaterials as amplified labels is beneficial for the construction of a biosensor with a high sensitivity.[20−23] Recently, MOF-derived nanomaterials are in the spotlight, in which MOFs are used as precursors and converted to various nanomaterials including porous carbon nanomaterials, metal or metal oxide/sulfide nanomaterials, and their composites, demonstrating a wide range of application including energy, catalysis, sensing, and biomedicine fields.[24−26] Traditional approaches for MOFs conversion are commonly based on pyrolysis or chemical reaction with specific reagents, which are ineluctably involved under harsh conditions (temperature, atmosphere, pH).[27,28] Recently, electrochemical approach with the advantages of simple, facile, and easily controllable has been focused, which opens a new path for MOFs conversion.[29] Motivated by the above considerations, the electrochemical inputs applied at the electrode surface are utilized with MOFs as a porous metal precursor to achieve fine control for the conversion of MOFs, which provide more options for the construction of MOF-based electrochemical devices.

Herein, a novel electrochemical biosensing platform was proposed based on a multipedal PDANs-DNA nanomachine and MOFs (NH_2-MIL-88(Fe)) decorated on DNA dendrimers for electrochemical conversion (Scheme 1). First, by the strength of Ca^{2+}-mediated DNA adsorption and target-triggered catalytic hairpin assembly (CHA), the multipedal PDANs-DNA nanomachine was constructed. With H1 adsorbed on PDANs through its A_{15} terminal via Ca^{2+}-mediated DNA adsorption to form PDANs-Ca^{2+}-H1 (Figure S1), the target miRNA-21 triggered the CHA on PDANs through matching with H1 to induce the assembly of H2, which formed the multipedal PDANs-DNA nanomachine (PDANs-Ca^{2+}-H1-H2) with miRNA-21 released for recycling. Then, the formed PDANs-DNA nanomachine moved fast on the electrode under Exo III driving, which utilized multiple legs simultaneously hybridized with DNA track to improve the walking efficiency. DNA track on electrode was selectively cleaved by Exo III, with the remaining sequence participated in the formation of DNA dendrimers. The cascade hybridization

https://doi.org/10.1021/acs.analchem.1c02125
Anal. Chem. 2021, 93, 13475−13484

of A1 and A2 formed the DNA dendrimers with abundant assembly sites for the MOFs probe. Finally, the decorated MOFs acted as a porous metal precursor for electrochemical conversion, resulting in electroactive Prussian Blue (PB) in situ generated on MOFs to produce an amplified signal. The mechanism was summarized as follows: (1) Electrochemical input with a high potential applied on the electrode surface was used for water-splitting reaction, which caused the generation of H^+ on the electrode surface; (2) the generated H^+ created an acid microenvironment and induced the dissociation of MOFs to release Fe^{3+}; (3) with the applied low potential, Fe^{3+} and $Fe(CN)_6^{3-}$ were electrochemically reduced into Fe^{2+} and $Fe(CN)_6^{4-}$, respectively; (4) Fe^{2+} and $Fe(CN)_6^{4-}$ reacted to generate Prussian White (PW); and (5) PW was oxidized by O_2 in the environment, resulting in the formation of PB. The detailed electrochemical conversion mechanism is expressed in Figure S2.

EXPERIMENTAL SECTION

Materials and Reagents. Dopamine hydrochloride, $FeCl_3{\cdot}6H_2O$, 2-aminoterephthalic acid (NH_2-BDC), sodium hydroxide (NaOH), calcium chloride ($CaCl_2$), tris-(hydroxymethyl)aminomethane (Tris), mercapto-1-hexanol (MCH), *N*-ethyl-*N*′-(3-dimethylaminopropyl)carbodiimide hydrochloride (EDC), potassium ferricyanide ($K_3[Fe(CN)_6]$), tris(2-carboxyethyl)phosphinehydrochloride (TCEP), gold chloride trihydrate ($HAuCl_4$), methylene blue (MB), K_2SO_4, and *N*-hydroxysuccinimide (NHS) were provided by Aladdin Co. (Shanghai, China). Exonuclease III (Exo III) was purchased from New England Biolabs (Beijing China). MicroRNA and oligonucleotides (Table S1) were received from Sangon Biotech Co., Ltd (Shanghai, China). Eastep Super Total RNA Extraction Kit was purchased from Shanghai Promega. Deionized water (electric resistance > 18.25 MΩ cm) was used to prepare the solutions in the experiments.

Apparatus and Measurements. Transmission electron microscopy (TEM) and high-angle annular dark-field scanning transmission electron microscopy (HAADF-STEM) with energy-dispersive X-ray spectroscopy (EDX) were carried out on a Talos F200S transmission electron microscope (FEI Company). Scanning electron microscopy (SEM) images were obtained with an SU8010 scanning electron microscope (HITACHI Ltd, Japan). ζ-Potential and dynamic light scattering (DLS) were detected by Zetasizer Nano ZS90 (Malvern, Britain). X-ray diffraction (XRD) was measured with a SmartLab X-ray diffractometer (Rigaku Co., Japan). A UV-3600 spectrophotometer (Shimadzu, Japan) was used to record UV−vis spectrum. An Escalab 250Xi X-ray photoelectron spectrometer (XPS, Thermo Fisher Scientific) was applied to X-ray photoelectron spectroscopy (XPS) characterization. The Bio-Rad XR+ Gel imaging system (Bio-Rad) was used to record the polyacrylamide gel electrophoresis (PAGE) image. Laser scanning confocal microscopy (LSCM) was performed on an LSM 900 microscope (ZEISS, Germany). Atomic force microscopy (AFM) was measured on a Dimension Edge atomic force microscope (Bruker Co., Germany). On the CHI 660E electrochemical workstation (Shanghai CH Instruments, China), electrochemical measurements including cyclic voltammetry (CV), differential pulse voltammetry (DPV), and electrochemical impedance spectroscopy (EIS) were performed with a modified gold electrode (GE), a platinum electrode, and a saturated calomel electrode (SCE). The scan rate and sample interval of CV were 100 mV/s and 0.001 V, respectively. The frequency of EIS was from 0.1 to 10^5 Hz with the initial potential of 0.208 V. The DPV of the biosensor was measured from −0.05 to 0.45 V with the amplitude, pulse width, and pulse period of 0.05 V, 0.05, and 0.2 s, respectively.

Fabrication of PDANs-DNA Nanomachine. PDANs were synthesized according to the reported method with some modification.[30] First, 40.5 mg of dopamine hydrochloride was dissolved in 10 mL of H_2O. Next, the above solution was mixed with 380 μL of NaOH (0.5 M) and vigorously stirred for 5 h at 50 °C. The obtained PDANs were centrifugated at 10 000 rpm and then redispersed in ultrapure water after washing three times. The synthesized PDANs were applied for the preparation of a PDANs-DNA nanomachine via Ca^{2+}-mediated DNA adsorption.[17] First, 50 μL of H1 (10 μM) was quickly added to 1 mL of PDANs containing 15 mM $CaCl_2$ and stirred for 5 min; the obtained PDANs-Ca^{2+}-H1 was collected by centrifugation and redispersed in Tris-HCl (10 mM, pH 7.4). Next, 25 μL of PDANs-Ca^{2+}-H1 was incubated with a mixture of 5 μL of a certain concentration of miRNA-21 and 20 μL of H2 (1 μM) for 1.5 h to form the multipedal PDANs-DNA nanomachine (PDANs-Ca^{2+}-H1-H2).

Synthesis of MOFs Probe. The MOFs (NH_2-MIL-88(Fe)) were synthesized according to the reported method with slight modification.[31] First, 0.374 g of $FeCl_3{\cdot}6H_2O$, 0.252 g of NH_2-BDC, and 10 μL of acetic acid were dissolved in 30 mL of dimethylformamide (DMF) with ultrasonic treatment for 30 min. Then, the mixture solution was reacted in a Teflon-lined reactor at 120 °C for 24 h. After centrifugated and washed three times with DMF and ethanol, the synthesized MOFs were vacuum-dried and used to prepare the MOFs probe as follows: 1 mL of MOFs (10 mg/mL) was added into the mixture solution of 400 mM EDC, 100 mM NHS, and 100 μL of P-DNA (10 μM), the mixture was reacted for 3 h and collected by centrifugation, and finally, the obtained MOFs probe was stored in Tris-HCl (10 mM, pH 7.4).

Preparation of the Biosensor. First, bare GE was polished and ultrasonically cleaned by ultrapure water and ethanol, followed by scanning in 0.5 M H_2SO_4 from −0.2 to 1.6 V. Then, the cleaned GE was immersed in 1 μM DNA track containing 0.2 mM TCEP for 12 h. After incubated with 1 mM MCH for 1 h, the modified electrode was treated with the mixture solution containing PDANs-DNA nanomachine and 20 U Exo III for 40 min. Then, the electrode was washed adequately and incubated with A1 (1 μM), and then the mixture of A1 (1 μM) and A2 (1 μM) was incubated for 1.5 h at 37 °C. Then, the electrode was treated with 50 μL of MOFs probe for 1 h at 37 °C. Finally, the biosensor was applied for electrochemical conversion in the solution containing 0.4 mM $K_3Fe(CN)_6$ and 0.1 M K_2SO_4, followed by a potential of 1.6 V scanned for 600 s and a potential of 0 V scanned for 300 s, and the sample interval was 0.002 s. The DPV response of the biosensor was measured in the solution containing 0.1 M HCl and 0.1 M K_2SO_4.

RNA Extraction from Cancer Cells. The Eastep Super Total RNA Extraction Kit was applied to extract total RNA from human breast cancer cells (MCF-7) and human cervical cancer cells (HeLa). First, the cancer cells were treated with 1 mL of tyrosine, then 0.5 mL of ethanol was added into the above solution, and centrifugated at 12 000 rpm for 1 min to collect the supernatant. After washing with 600 μL of RNA lotion, the supernatant in adsorption film was incubated with

https://doi.org/10.1021/acs.analchem.1c02125
Anal. Chem. 2021, 93, 13475−13484

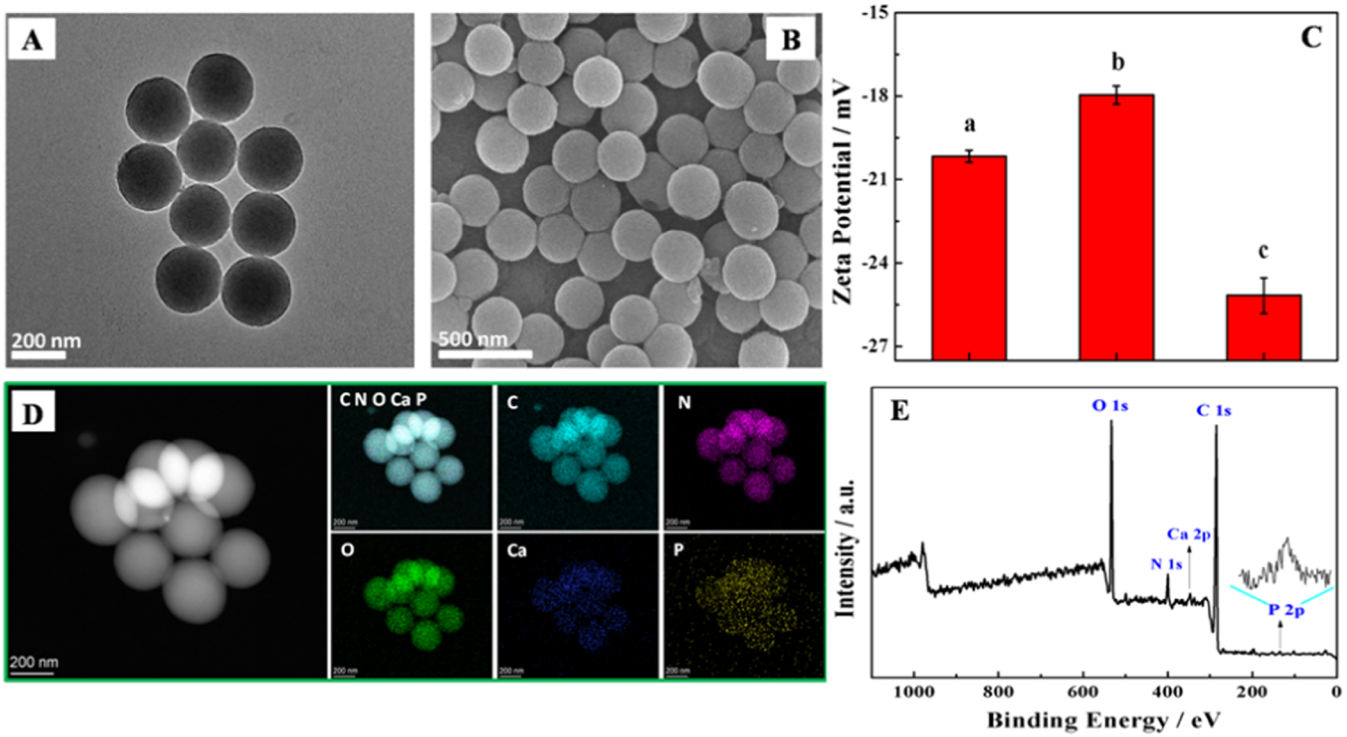

Figure 1. (A) TEM and (B) SEM image of PDANs. (C) ζ-Potential of (a) PDANs, (b) PDANs incubated with Ca^{2+}, and (C) Ca^{2+}-mediated PDANs-DNA nanomachine. (D) HAADF-STEM image of PDANs-DNA nanomachine and the corresponding elemental mapping of C, N, O, Ca, and P elements. (E) XPS spectrum of PDANs-DNA nanomachine.

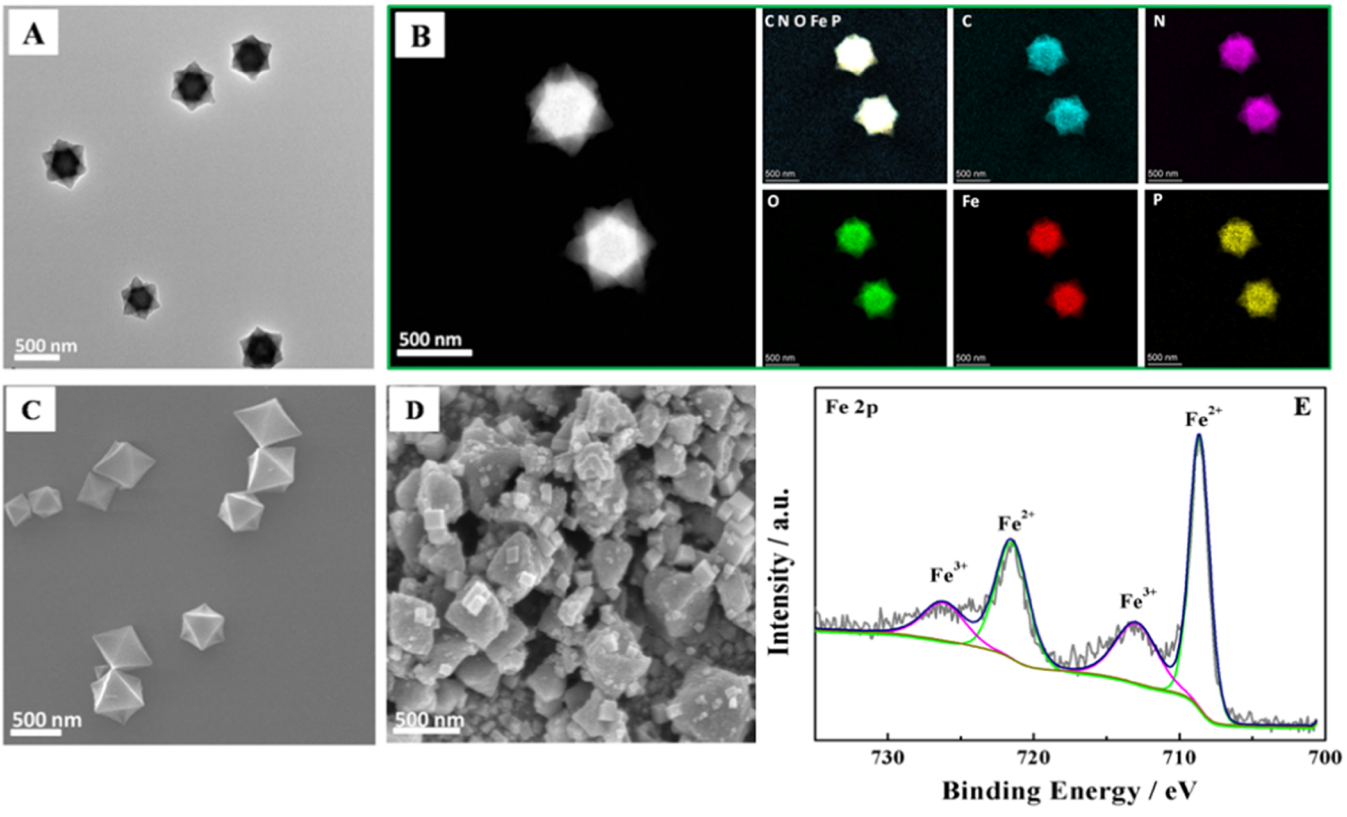

Figure 2. (A) TEM image of MOFs (NH_2-MIL-88 (Fe)). (B) HAADF-STEM image of MOFs probe and the corresponding elemental mapping of C, N, O, Fe, and P elements. (C) SEM image of MOFs. (D) SEM image of MOFs after electrochemical conversion. (E) XPS spectrum of Fe 2p of MOFs after electrochemical conversion.

https://doi.org/10.1021/acs.analchem.1c02125
Anal. Chem. 2021, 93, 13475−13484

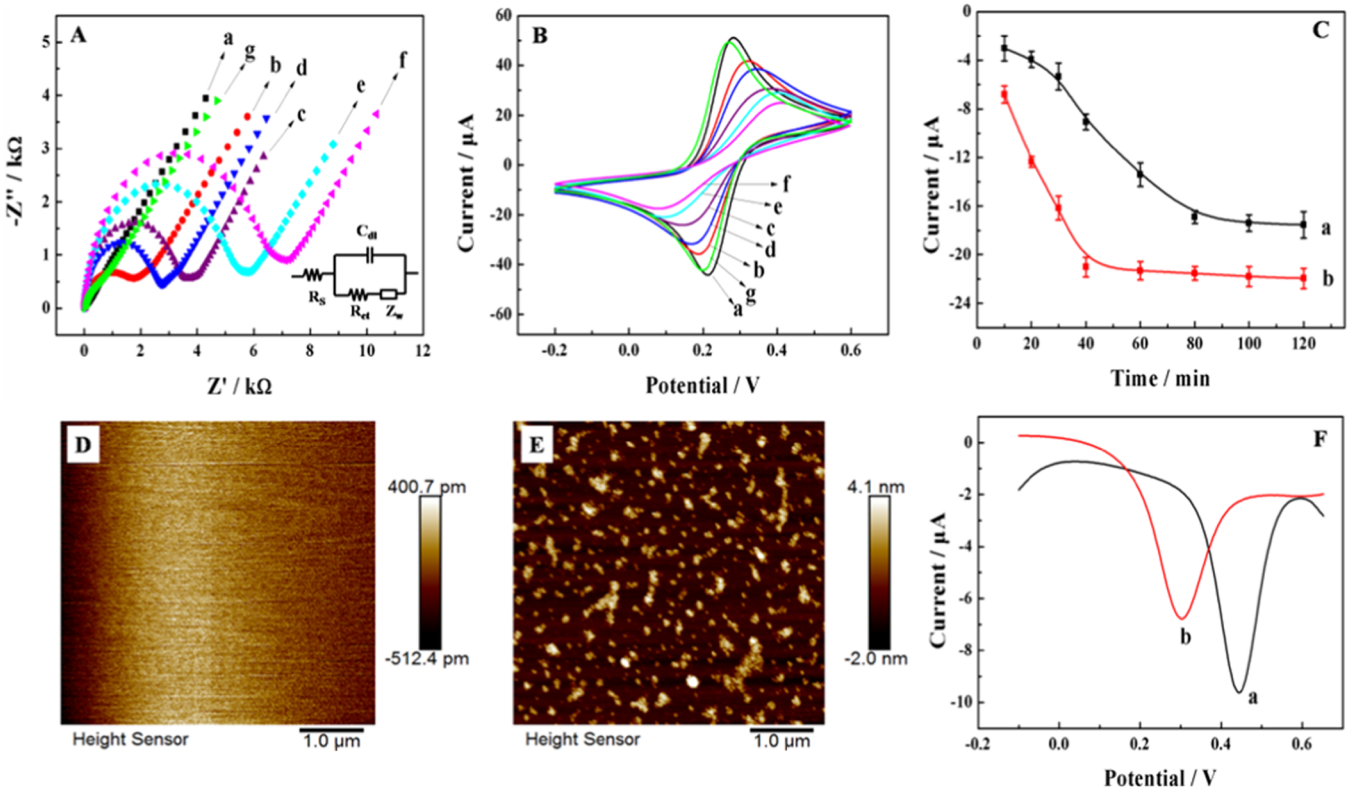

Figure 3. (A) EIS and (B) CV curves of the biosensor of miRNA-21 with stepwise modification: (a) bare GE, (b) DNA track/GE, (c) MCH/DNA track/GE, (d) c incubated with PDANs-DNA nanomachine and Exo III, (e) d hybridized with A1 and A2, (f) e incubated with MOFs probe, and (g) e after electrochemical conversion. (C) Walking efficiency of the multipedal PDANs-DNA nanomachine compared with H1-H2 DNA walker. (D) AFM image of bare mica. (E) AFM image of the formed DNA dendrimers. (F) DPV curves of GE in solution (pH 1.6) of 0.1 M K_2SO_4 containing (a) 0.1 M $FeCl_3$ and (b) 0.1 M $K_3Fe(CN)_6$.

50 μL of DNase I for 15 min at room temperature. After washing twice with RNA lotion, the obtained RNA was stored in 50 μL of nuclease-free water and stored at −20 °C for further use.

RESULTS AND DISCUSSION

Characterization of Nanomaterials. The synthesized PDANs and PDANs-DNA nanomachine were characterized. As shown in Figure 1A, uniform PDANs were observed with a diameter of about 250 nm. In addition, the PDANs were globular particles in shape (Figure 1B). The UV−vis absorption spectra of PDANs showed a characteristic absorption peak at 235 nm (Figure S3).[32] Furthermore, the formation of PDANs-DNA nanomachine was validated by ζ-potential. As demonstrated in Figure 1C, the ζ-potential of PDANs was −20.2 mV (a), which increased to −18.2 mV after incubated with Ca^{2+} (b), while the Ca^{2+}-coordinated PDANs were still negatively charged. With the formation of PDANs-DNA nanomachine, the ζ-potential decreased to −24.7 mV (c), which was owing to the assembly of negative charged DNA. DLS analysis confirmed that the peak of PDANs was at about 260 nm, which shifted to 298 nm after the Ca^{2+}-mediated DNA adsorption, indicating the formation of PDANs-DNA nanomachine (Figure S4). Besides, EDX analysis was performed to further verify the PDANs-DNA nanomachine. As displayed in Figure 1D, the elemental mappings revealed the uniform distribution of C (cyan zone), N (purple zone), O (green zone), Ca (blue zone), and P (yellow zone) elements in PDANs-DNA nanomachine, and the presence of Ca and P was attributed to the Ca^{2+} coordination and DNA adsorption. Moreover, XPS was used to confirm the PDANs-DNA nanomachine (Figure 1E). Five peaks representing C (285.1 eV), N (399.1 eV), O (531.7 eV), Ca (346.1 eV), and P (133.5 eV) could be observed, and the peaks of Ca and P were attributed to the Ca^{2+}-mediated DNA adsorption on PDANs. The stability of the PDANs-DNA nanomachine (Figure S5) and that formed with different concentrations of Ca^{2+} (Figure S6) were also explored, indicating the good stability of PDANs-DNA nanomachine.

In addition, the synthesized MOFs (NH_2-MIL-88(Fe)) and the MOFs probe were characterized. As displayed in Figure 2A, the TEM image revealed the polyhedral morphology of the synthesized MOFs with the average size of about 500 nm. XRD was applied to confirm the crystallographic structure of MOFs (Figure S7). It could be seen that the main diffraction peaks of the synthesized MOFs were in agreement with the simulated diffraction peaks of NH_2-MIL-88(Fe), indicating the successful synthesis of MOFs. Moreover, EDX analysis was used to characterize the MOFs probe. As demonstrated in Figure 2B, the elemental mappings displayed the C (blue zone), N (purple zone), O (green zone), Fe (red zone), and P (yellow zone) elements. These elements were homogeneously distributed throughout the MOFs, and the presence of the P element proved the successful modification of P-DNA on the MOFs. Furthermore, the morphology of MOFs before and after electrochemical conversion was investigated. As presented in Figure 2C, the synthesized MOFs showed the typical octahedral morphology.[33] After electrochemical conversion, it could be observed that the crystal structures of MOFs were

https://doi.org/10.1021/acs.analchem.1c02125
Anal. Chem. 2021, 93, 13475−13484

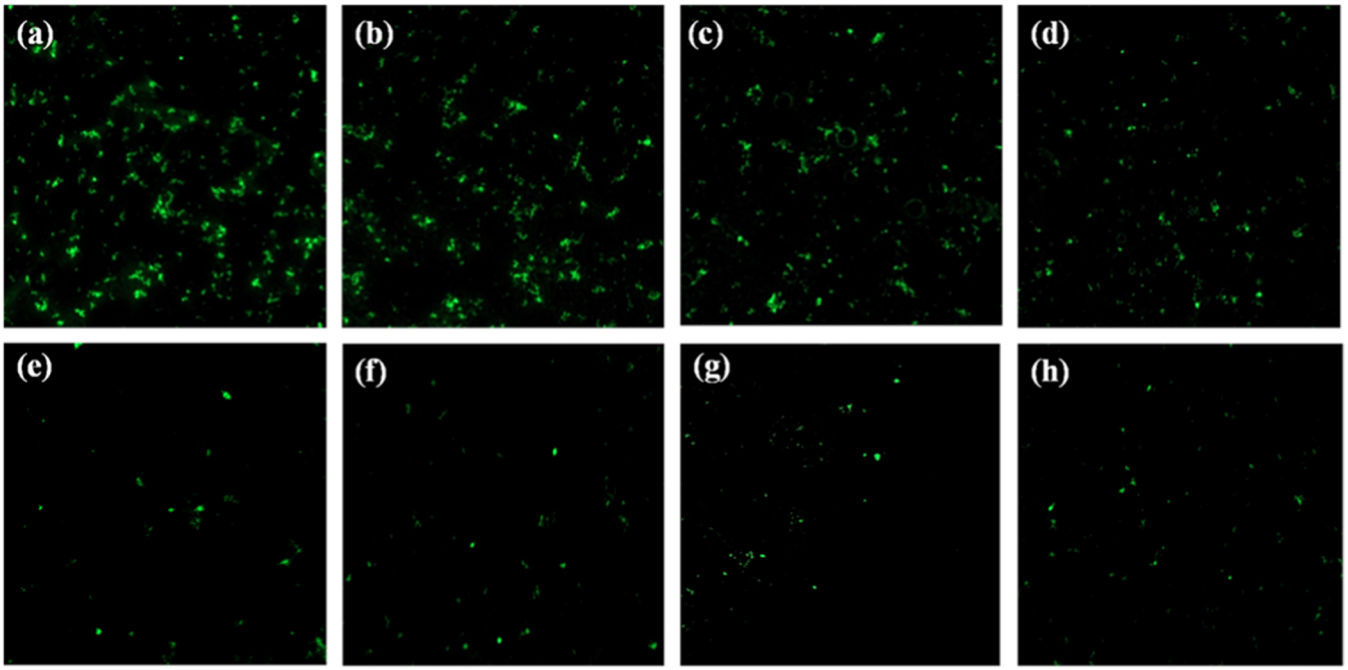

Figure 4. LSCM images of the PDANs-DNA nanomachine walking processs on FAM-DNA track-modified AuNPs/ITO electrode: (a) 0 min, (b) 10 min, (c) 20 min, (d) 30 min, (e) 40 min, (f) 50 min, (g) 60 min, (h) 70 min.

damaged and cubic PB was in situ formed on the surface of MOFs (Figure 2D). Moreover, XPS was used to confirm the generation of PB after electrochemical conversion. The survey spectra of MOFs before and after the electrochemical conversion are presented in Figure S8, which demonstrated the peaks corresponding to C 1s, N 1s, O 1s, and Fe 2p. In the Fe 2p spectrum, the MOFs presented the binding energy of Fe $2p_{1/2}$ (725.2 eV) and Fe $2p_{3/2}$ (711.6 eV) before electrochemical conversion, which proved the presence of Fe^{3+} in MOFs (Figure S9). After electrochemical conversion, the Fe 2p spectra with the binding energies of Fe $2p_{1/2}$ (726.2 eV) and Fe $2p_{3/2}$ (713.1 eV) were ascribed to Fe^{3+} and the peaks of Fe $2p_{1/2}$ (721.5 eV) and Fe $2p_{3/2}$ (708.6 eV) were attributed to the presence of Fe^{2+}, which proved the formation of PB (Figure 2E).[34]

Characterization of the Biosensor. The stepwise modification of the biosensor was verified by EIS and CV in 5 mM $[Fe(CN)_6]^{3-/4-}$ containing 0.1 M KCl. The equivalent circuit was applied for EIS analysis, in which R_s, R_{et}, C_{dl}, and Z_w represent the electrolyte resistance, electron-transfer resistance, double-layer capacitance, and Warburg impedance, respectively. As exhibited in Figure 3A, the DNA track-modified GE (curve b) showed a greater R_{et} (2044 Ω) compared with R_{et} (218 Ω) of bare GE (curve a) because the modified DNA track hindered the electron transfer. The R_{et} (3852 Ω) value further increased with the immobilization of MCH (curve c). After the accomplishment of PDANs-DNA nanomachine walking process, R_{et} (2742 Ω) decreased because the DNA track was partially cleaved by Exo III (curve d). With the cascade assembly of A1 and A2, R_{et} (5711 Ω) increased obviously (curve e) on account of the formation of DNA dendrimers. The R_{et} (7190 Ω) value kept increasing with the hybridization of MOFs probe (curve f). After the electrochemical conversion process, R_{et} (415 Ω) markedly decreased with the in situ formation of electroactive PB (curve g). In addition, CV curves of the modification process were in accordance with the EIS results, proving the biosensor was constructed successfully (Figure 3B). Besides, the DNA hybridization process of the biosensor was verified by PAGE analysis, which indicated the successful implement of CHA, Exo III cleavage process, the formation of DNA dendrimers, and the assembly of P-DNA on DNA dendrimers (Figure S10). The NUPACK analysis further proved the DNA hybridization of the biosensor (Figure S11). Moreover, the successful implementation of the PDANs-DNA nanomachine walking process and the two hairpins assembly were proved using adsorbed MB as signal molecules (Figure S12).

To examine the walking performance of multipedal PDANs-DNA nanomachine, the walking efficiency of PDANs-DNA nanomachine was compared with traditional step-by-step DNA walker (H1-H2). H1-H2 DNA walker was designed without the presence of PDANs, and miRNA-21 triggered the CHA process to form H1-H2 DNA walker, which only utilized one leg to achieve the step-by-step walking on the electrode under Exo III driving. As exhibited in Figure 3C, H1-H2 DNA walker showed an increase of DPV response with the increase of incubation time, and it achieved a platform at 80 min (curve a). Nevertheless, the PDANs-DNA nanomachine achieved a faster and stronger increase of DPV response, which became stable at 40 min (curve b). The higher walking efficiency of PDANs-DNA nanomachine was because of the multiple legs simultaneously walked under Exo III driving, which obviously improved the walking efficiency. Furthermore, the kinetics of PDANs-DNA nanomachine was investigated in Figure S13, indicating that the walking process was related to the target-induced formation of multiple legs, which improved the walking efficiency. Besides, the size of PDANs was controlled and is presented in Figure S14. The walking efficiency of the PDANs-DNA nanomachine with different sizes was investigated, and the PDANs-DNA nanomachine used in the experiment with the diameter of 250 nm exhibited a satisfying walking efficiency (Figure S15).

https://doi.org/10.1021/acs.analchem.1c02125
Anal. Chem. 2021, 93, 13475−13484

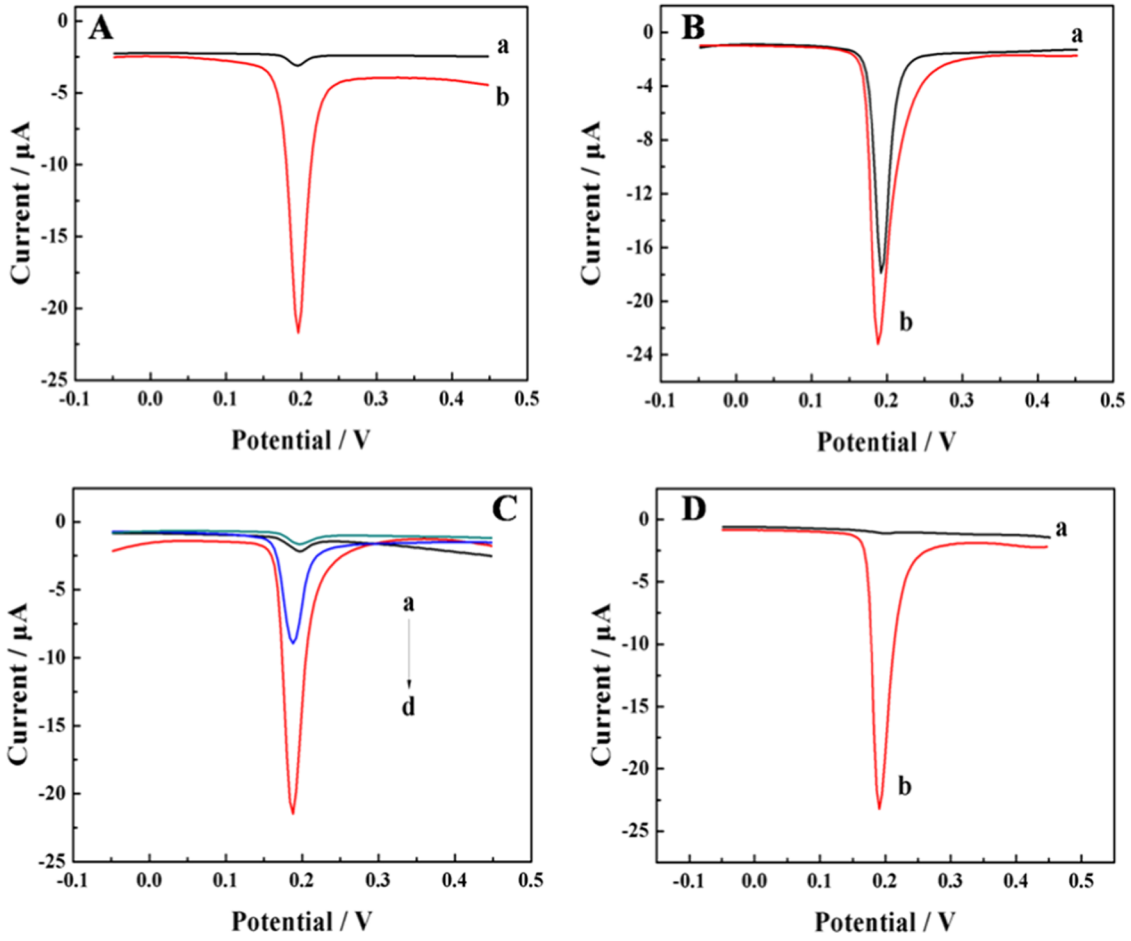

Figure 5. Amplification performance of the biosensor: (A) electrochemical response without (a) and with (b) the CHA process. (B) Electrochemical signal without (a) and with (b) the presence of PDANs. (C) DPV response (a) without A1 and A2, (b) without A1, (c) without A2, and (d) with A1 and A2. (D) DPV signal before (a) and after (b) the electrochemical conversion process.

The formation of DNA dendrimers was further verified by AFM. As shown in Figure 3D, the bare mica presented a clean and flat surface. After the assembly A1 and A2, a large amount of DNA nanostructures could be observed on the mica, indicating the successful cascade hybridization of the two hairpins (Figure 3E). To reveal the formation mechanism of PB, the electrochemical method was applied to investigate the reduction process of Fe^{3+} and $Fe(CN)_6^{3-}$. As demonstrated in Figure 3F, the reduction of Fe^{3+} to Fe^{2+} commenced at 0.6 V and the reduction of $Fe(CN)_6^{3-}$ to $Fe(CN)_6^{4-}$ commenced at 0.5 V. Therefore, only the reduction of Fe^{3+} to Fe^{2+} occurred with the potential of 0.5−0.6 V. With the potential below 0.5 V, the electrochemical reduction of Fe^{3+} and $Fe(CN)_6^{3-}$ to Fe^{2+} and $Fe(CN)_6^{4-}$ took place simultaneously. The electrochemically reduced Fe^{2+} and $Fe(CN)_6^{4-}$ reacted to form PW and finally oxidized to PB.

LSCM Image of PDANs-DNA Nanomachine Walking Process. The walking process of PDANs-DNA nanomachine was also recorded by LSCM. First, gold nanoparticle-deposited indium tin oxide electrode (AuNPs/ITO) was obtained by scanning ITO in 1% $HAuCl_4$ solution at −0.2 V for 60 s, and the deposited AuNPs were about 300−500 nm (Figure S16). Then, 6-carboxyfluorescein-labeled DNA track (FAM-DNA track) was immobilized on AuNPs/ITO and the PDANs-DNA nanomachine walking process was performed. As displayed in Figure 4, it could be observed that the FAM-DNA track presented green fluorescence image, and the amount of fluorescence dots decreases with the increase of walking time, which became stable after 40 min. The decrease of fluorescence dots was attributed to the walking of the PDANs-DNA nanomachine that caused the cleavage of FAM-DNA track, proving the successful implementation of the PDANs-DNA nanomachine walking process.

Amplification Performance of the Biosensor. The effect of PDANs-DNA nanomachine was explored. First, the amplification effect of CHA was investigated. As exhibited in Figure 5A, the electrochemical signal was negligible without the CHA process (curve a). With the completion of CHA, a significant DPV response could be observed (curve b), which was attributed to the CHA process, resulting in the formation of multiple legs for PDANs-DNA nanomachine. Moreover, the effect of PDANs is verified in Figure 5B. Compared with the H1-H2 DNA walker (curve a), the multipedal PDANs-DNA nanomachine possessed greater DPV response (curve b), which was in virtue of the multiple legs increasing the amount of cleaved DNA track to participate in the formation of DNA dendrimers.

In addition, the effect of the DNA dendrimers for signal amplification was investigated. As displayed in Figure 5C, the biosensor had a negligible electrochemical signal without the addition of A1 and A2 (curve a). Without the presence of A1, the DPV response had no obvious increase because there was

https://doi.org/10.1021/acs.analchem.1c02125
Anal. Chem. 2021, 93, 13475−13484

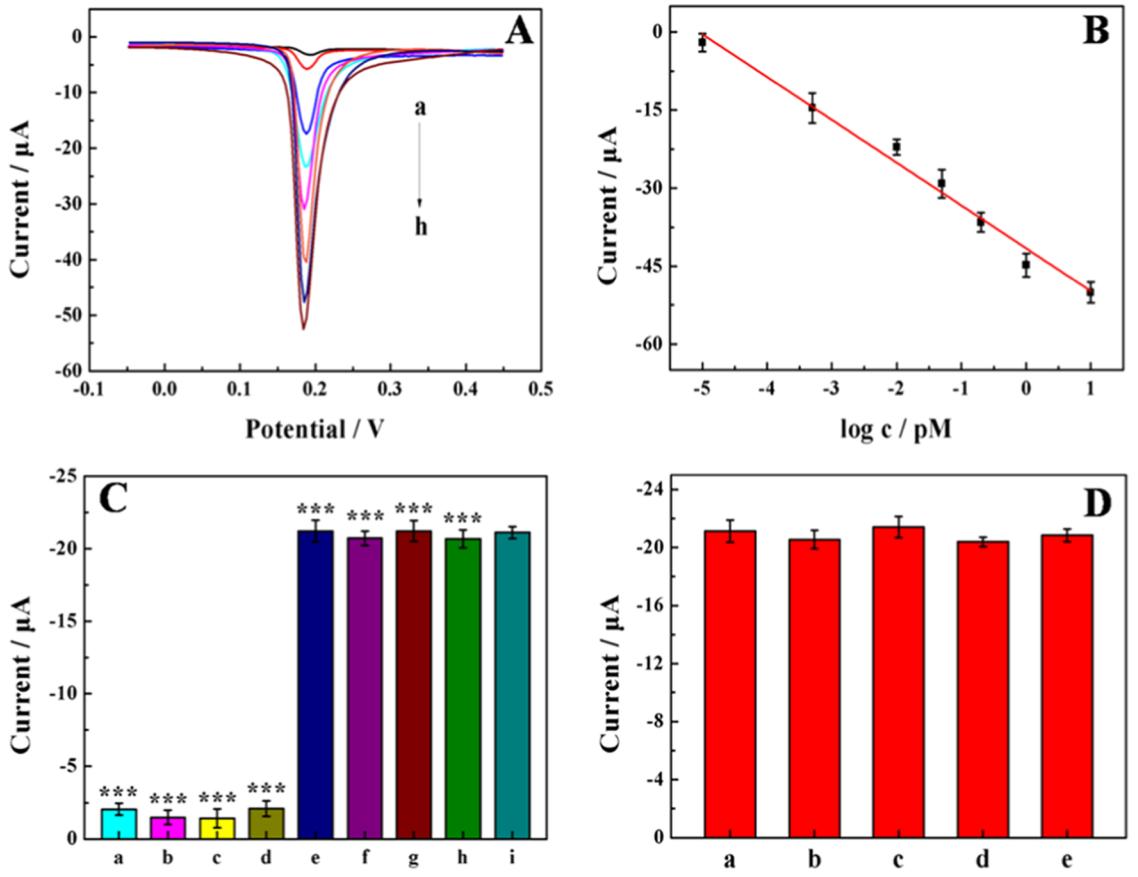

Figure 6. (A) DPV signals of the biosensor toward different miRNA-21 concentrations (from a−h: 0, 0.01, 0.5, 10 fM, 0.05, 0.2, 1, 10 pM). (B) Calibration plot of the biosensor for miRNA-21 detection. (C) Selectivity of the electrochemical biosensor toward miRNA-21 (10 fM) and interferences miRNA (100 fM): (a) miRNA-141, (b) miRNA-155, (c) miRNA-205, (d) miRNA let-7a, (e) miRNA-21 + miRNA-141, (f) miRNA-21 + miRNA-155, (g) miRNA-21 + miRNA-205, (h) miRNA-21 + miRNA let-7a, and (i) miRNA-21. Asterisks represent the statistically significant differences (***$p < 0.001$). (D) Electrochemical signal of five biosensors for 10 fM miRNA-21 detection.

no MOFs probe modified on the electrode (curve b). The DPV signal showed an obvious increase with the addition of A1, which was due to MOFs probe hybridized with A1 to produce signal (curve c). With the introduction of A1 and A2, the electrochemical signal of the biosensor increased significantly (curve d) because the alternate hybridization of A1 and A2 formed the DNA dendrimers, which provided abundant assembly sites for the MOFs probe.

Furthermore, the electrochemical conversion of MOFs for signal amplification was checked. As could be seen in Figure 5D, the electrochemical signal of the biosensor was inconspicuous without the electrochemical conversion process (curve a). After electrochemical conversion, a conspicuous DPV signal was observed (curve b) because the MOFs acted as a porous metal precursor and electrochemically converted into electroactive PB to produce an amplified signal.

Analytical Performance for miRNA-21 Detection. Under optimal experimental conditions (Figure S17), the analytical performance of the biosensor was examined by detecting different concentrations of miRNA-21. As shown in Figure 6A, increasing DPV current could be observed with the increase of miRNA-21 concentration, which was because increasing miRNA-21 led to the formation of more DNA dendrimers, resulting in more MOFs probe decorated on DNA dendrimers to produce signal. The calibration plot is displayed in Figure 6B, from which it could be seen that the DPV current of the biosensor kept good proportion with the logarithm of miRNA-21 concentrations in the range of 10 aM to 10 pM. The regression equation was I (μA) = $-8.231 \lg c - 41.56$ (pM) ($R = 0.9905$), and the detection limit was 5.8 aM (S/N = 3). The proposed biosensor was compared with the reported methods for miRNA-21 detection, and it was found that this strategy had higher sensitivity and possessed a lower detection limit (Table S2).[35−41]

To check the selectivity of the biosensor, the electrochemical response of the biosensor toward miRNA-21, four interferences (miRNA-141, miRNA-155, miRNA-205, miRNA let-7a), and their mixture was investigated. As shown in Figure 6C, the DPV response for the detection of 100 fM interfering miRNA was negligible, while a significant increase of the electrochemical response was recorded with the presence of 10 fM miRNA-21. In addition, the DPV signal of the biosensor toward the mixture of miRNA-21 and interfering miRNA revealed a similar electrochemical response compared with that of miRNA-21, confirming that the proposed biosensor had good selectivity. To verify the reproducibility, five similarly prepared electrodes were applied for the measurement of 10 fM miRNA-21 (Figure 6D). It was found that the DPV response of the five biosensors was similar with the relative standard deviation (RSD) of 3.1%, manifesting the accepted reproducibility of the biosensor. The stability of PDANs-DNA nanomachine-enabled biosensor was explored, which kept good stability after 2-week storage (Figure S18).

https://doi.org/10.1021/acs.analchem.1c02125
Anal. Chem. 2021, 93, 13475−13484

Real Sample Analysis. The application potential of the biosensor was investigated through the recovery test in biological samples (Table S3). By adding different concentrations (1, 0.5, 0.01 pM) of miRNA-21 into 10-fold diluted human serum, the recoveries for miRNA-21 detection ranged from 96.4 to 102.6% with the RSDs from 2.3 to 3.9%, which indicated the feasibility of the proposed biosensor for miRNA-21 detection in clinical sample analysis. To further confirm the application potential of the biosensor, miRNA-21 extracted from MCF-7 and HeLa cells were detected (Figure 7). The

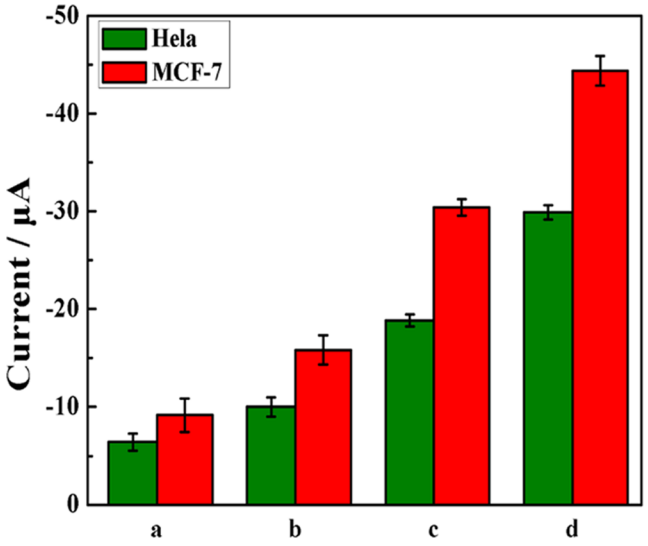

Figure 7. DPV response of the biosensor toward different numbers of HeLa and MCF-7 cells (from a–d: 100, 1000, 10 000, and 100 000).

electrochemical signal gradually increased with the increasing number of MCF-7 and HeLa cells ranging from 100 to 10 000, which was because the miRNA concentration was increased with increasing cell number. However, a stronger signal could be observed in MCF-7 cells, manifesting the higher expression of miRNA-21 in MCF-7 cells than in HeLa cells. The experimental results were consistent with the previous report,[42] proving that the biosensor held prospective application in disease diagnosis.

CONCLUSIONS

In conclusion, a novel electrochemical biosensing platform of miRNA-21 was designed based on a Ca^{2+}-mediated multipedal PDANs-DNA nanomachine with MOFs decorated on DNA dendrimers for electrochemical conversion. The proposed biosensor possessed three fascinating features: First, a multipedal PDANs-DNA nanomachine was constructed through Ca^{2+}-mediated DNA adsorption and target-induced CHA process, which was simple, label-free, and time-saving. Second, the PDANs-DNA nanomachine showed a high walking efficiency with multiple legs simultaneously walking on the electrode, resulting in the formation of DNA dendrimers for signal amplification. Third, the MOFs decorated on dendrimers acted as a porous metal precursor with electrochemical conversion to produce signal; this facile and controllable approach further improved the sensitivity. Therefore, the proposed strategy provided a compelling platform with efficient walking pattern and ingenious electrochemical conversion, holding promising application in clinical analysis and diagnosis.

ASSOCIATED CONTENT

Supporting Information

The Supporting Information is available free of charge at https://pubs.acs.org/doi/10.1021/acs.analchem.1c02125.

Mechanism of Ca^{2+}-mediated DNA adsorption on PDANs; electrochemical conversion mechanism of MOFs; UV–vis absorption spectra of PDANs; DLS analysis of PDANs and PDANs-DNA nanomachine; stability of PDANs-DNA nanomachine and that with different Ca^{2+} concentrations; XRD spectra of the synthesized MOFs; XPS survey spectra of MOFs before and after electrochemical conversion; XPS spectrum of Fe 2p of MOFs before electrochemical conversion; PAGE analysis of DNA hybridization process; NUPACK analysis for nucleic acid chain reactions; characterization of PDANs-DNA nanomachine walking process and hairpins assembly; kinetic study of PDANs-DNA nanomachine; SEM images of PDANs with different sizes and their walking efficiencies; SEM image of the AuNPs/ITO electrode; optimization of detection conditions; stability of the PDANs-DNA nanomachine-enabled biosensor; sequences of miRNA and the oligonucleotides; comparison of the proposed strategy with reported methods; and recovery test of the biosensor in human serum (PDF)

AUTHOR INFORMATION

Corresponding Author

Shengfu Wang – *Collaborative Innovation Center for Advanced Organic Chemical Materials Co-Constructed by the Province and Ministry, Ministry of Education Key Laboratory for the Synthesis and Application of Organic Functional Molecules, College of Chemistry and Chemical Engineering, Hubei University, Wuhan 430062, P. R. China;* orcid.org/0000-0001-7175-4908; Phone: +86-27-50865309; Email: wangsf@hubu.edu.cn; Fax: +86-27-88663043

Authors

Ting Bao – *Collaborative Innovation Center for Advanced Organic Chemical Materials Co-Constructed by the Province and Ministry, Ministry of Education Key Laboratory for the Synthesis and Application of Organic Functional Molecules, College of Chemistry and Chemical Engineering, Hubei University, Wuhan 430062, P. R. China*

Ruobing Fu – *Collaborative Innovation Center for Advanced Organic Chemical Materials Co-Constructed by the Province and Ministry, Ministry of Education Key Laboratory for the Synthesis and Application of Organic Functional Molecules, College of Chemistry and Chemical Engineering, Hubei University, Wuhan 430062, P. R. China*

Yuying Jiang – *Collaborative Innovation Center for Advanced Organic Chemical Materials Co-Constructed by the Province and Ministry, Ministry of Education Key Laboratory for the Synthesis and Application of Organic Functional Molecules, College of Chemistry and Chemical Engineering, Hubei University, Wuhan 430062, P. R. China*

Wei Wen – *Collaborative Innovation Center for Advanced Organic Chemical Materials Co-Constructed by the Province and Ministry, Ministry of Education Key Laboratory for the Synthesis and Application of Organic Functional Molecules, College of Chemistry and Chemical Engineering, Hubei*

University, Wuhan 430062, P. R. China; orcid.org/0000-0001-6138-7470

Xiuhua Zhang − *Collaborative Innovation Center for Advanced Organic Chemical Materials Co-Constructed by the Province and Ministry, Ministry of Education Key Laboratory for the Synthesis and Application of Organic Functional Molecules, College of Chemistry and Chemical Engineering, Hubei University, Wuhan 430062, P. R. China;* orcid.org/0000-0003-3586-9921

Complete contact information is available at: https://pubs.acs.org/10.1021/acs.analchem.1c02125

Notes

The authors declare no competing financial interest.

■ ACKNOWLEDGMENTS

This work was funded by the National Natural Science Foundation of China (Grant No. 21775033).

■ REFERENCES

(1) Zhang, P.; Jiang, J.; Yuan, R.; Zhuo, Y.; Chai, Y. Q. *J. Am. Chem. Soc.* **2018**, *140*, 9361−9364.
(2) Yang, X.; Tang, Y.; Mason, S. D.; Chen, J.; Li, F. *ACS Nano* **2016**, *10*, 2324−2330.
(3) Peng, R. Z.; Zheng, X. F.; Lyu, Y. F.; Xu, L. J.; Zhang, X. B.; Ke, G. L.; Liu, Q. L.; You, C. J.; Huan, S. Y.; Tan, W. H. *J. Am. Chem. Soc.* **2018**, *140*, 9793−9796.
(4) Qu, X. M.; Zhu, D.; Yao, G. B.; Su, S.; Chao, J.; Liu, H. J.; Zuo, X. L.; Wang, L. H.; Shi, J. Y.; Wang, L. H.; Huang, W.; Pei, H.; Fan, C. H. *Angew. Chem., Int. Ed.* **2017**, *129*, 1881−1884.
(5) Xu, X. W.; Wang, L.; Li, K.; Huang, Q. H.; Jiang, W. *Anal. Chem.* **2018**, *90*, 3521−3530.
(6) Kay, E. R.; Leigh, D. A.; Zerbetto, F. *Angew. Chem., Int. Ed.* **2007**, *46*, 72−191.
(7) Yang, X. L.; Tang, Y. N.; Mason, S. D.; Chen, J. B.; Li, F. *ACS Nano* **2016**, *10*, 2324−2330.
(8) Liang, C. P.; Ma, P. Q.; Liu, H.; Guo, X. G.; Yin, B. C.; Ye, B. C. *Angew. Chem., Int. Ed.* **2017**, *129*, 9205−9209.
(9) Li, N. X.; Zheng, J.; Li, C. R.; Wang, X. X.; Ji, X. H.; He, Z. K. *Chem. Commun.* **2017**, *53*, 8486−8488.
(10) He, C. B.; Liu, D. M.; Lin, W. B. *Chem. Rev.* **2015**, *115*, 11079−11108.
(11) Liu, Y.; Ai, K.; Lu, L. *Chem. Rev.* **2014**, *114*, 5057−5115.
(12) Poinard, B.; Neo, S. Z. Y.; Yeo, E. L. L.; Heng, H. P. S.; Neoh, K. G.; Kah, J. C. Y. *ACS Appl. Mater. Interfaces* **2018**, *10*, 21125−21136.
(13) Deng, X. X.; Wu, S.; Li, Z. P.; Zhao, Y. Q.; Duan, C. Y. *Anal. Chem.* **2020**, *92*, 15908−15915.
(14) Qiang, W. B.; Hu, H. T.; Sun, L.; Li, H.; Xu, D. K. *Anal. Chem.* **2015**, *87*, 12190−12196.
(15) He, D.; He, X.; Yang, X.; Li, H. W. *Chem. Sci.* **2017**, *8*, 2832−2840.
(16) Wang, Z.; Xie, Y. J.; Li, Y. W.; Huang, Y. R.; Parent, L. R.; Ditri, T.; Zang, N.; Rinehart, J. D.; Gianneschi, N. C. *Chem. Mater.* **2017**, *29*, 8195−8201.
(17) Meng, Y. C.; Liu, P.; Zhou, W. H.; Ding, J. S.; Liu, J. W. *ACS Nano* **2018**, *12*, 9070−9080.
(18) Zhou, H. C.; Kitagawa, S. *Chem. Soc. Rev.* **2014**, *43*, 5415−5418.
(19) Howarth, A. J.; Liu, Y. Y.; Li, P.; Li, Z. Y.; Wang, T. C.; Hupp, J. T.; Farha, O. K. *Nat. Rev. Mater.* **2016**, *1*, No. 15018.
(20) Zhang, W.; Wang, X.; Li, P.; Zhang, W.; Wang, H.; Tang, B. *Anal. Chem.* **2020**, *92*, 8952−8958.
(21) Bao, T.; Fu, R. B.; Wen, W.; Zhang, X. H.; Wang, S. F. *ACS Appl. Mater. Interfaces* **2020**, *12*, 2087−2094.
(22) Zhang, Q.; Li, L. Y.; Qiao, Z. H.; Lei, C. Y.; Fu, Y. C.; Xie, Q. J.; Yao, S. Z.; Li, Y. B.; Ying, Y. B. *Anal. Chem.* **2017**, *89*, 12145−12151.
(23) Sun, Z. W.; Wang, L.; Wu, S.; Pan, Y. H.; Dong, Y.; Zhu, S.; Yang, J.; Yin, Y. M.; Li, G. X. *Anal. Chem.* **2020**, *92*, 3819−3826.
(24) Yang, W. P.; Li, X. X.; Li, Y.; Zhu, R. M.; Pang, H. *Adv. Mater.* **2019**, *31*, No. 1804740.
(25) Zhang, Y. X.; Xu, J. Y.; Xia, J. F.; Zhang, F. F.; Wang, Z. H. *ACS Appl. Mater. Interfaces* **2018**, *10*, 39151−39160.
(26) Yao, L.; Gu, Q. F.; Yu, X. B. *ACS Nano* **2021**, *15*, 3228−3240.
(27) Yilmaz, G.; Yam, K. M.; Zhang, C.; Fan, H. J.; Ho, G. W. *Adv. Mater.* **2017**, *29*, No. 1606814.
(28) Wang, D. D.; Jana, D.; Zhao, Y. L. *Acc. Chem. Res.* **2020**, *53*, 1389−1400.
(29) He, W. H.; Ifraemov, R.; Raslin, A.; Hod, I. *Adv. Funct. Mater.* **2018**, *28*, No. 1707244.
(30) Ju, K. Y.; Lee, Y.; Lee, S.; Park, S. B.; Lee, J. K. *Biomacromolecules* **2011**, *12*, 625−632.
(31) Xie, D. H.; Ma, Y.; Gu, Y.; Zhou, H. J.; Zhang, H. M.; Wang, G. Z.; Zhang, Y. X.; Zhao, H. J. *J. Mater. Chem. A* **2017**, *5*, 23794−23804.
(32) Xiao, T.; Sun, J.; Zhao, J. H.; Wang, S.; Liu, G. Y.; Yang, X. R. *ACS Appl. Mater. Interfaces* **2018**, *10*, 6560−6569.
(33) Sun, Z.; Fan, Y. Z.; Du, S. Z.; Yang, Y. Z.; Ling, Y.; Li, N. B.; Luo, H. Q. *Anal. Chem.* **2020**, *92*, 7273−7281.
(34) Guo, L.; Zhang, Y. J.; Yu, Y. L.; Wang, J. H. *Anal. Chem.* **2020**, *92*, 14806−14813.
(35) Liu, W.; Chen, A. Y.; Li, S. K.; Peng, K. F.; Chai, Y. Q.; Yuan, R. *Anal. Chem.* **2019**, *91*, 1516−1523.
(36) Gao, Y. H.; Wang, J.; Wang, W. N.; Zhao, T. T.; Cui, Y. Y.; Liu, P. P.; Xu, S. H.; Luo, X. L. *Anal. Chem.* **2021**, *93*, 2480−2489.
(37) Wang, G. X.; Han, R.; Li, Q.; Han, Y. F.; Luo, X. L. *Anal. Chem.* **2020**, *92*, 7186−7193.
(38) Chu, X. Y.; Wu, R.; Fan, G. C.; Deng, A. P.; Zhu, J. J. *ACS Sustainable Chem. Eng.* **2018**, *6*, 11633−11641.
(39) Zhou, Z. X.; Sohn, Y. S.; Nechushtai, R.; Willner, I. *ACS Nano* **2020**, *14*, 9021−9031.
(40) Ma, X. Y.; Chen, X. F.; Tang, Y. G.; Yan, R. H.; Miao, P. *ACS Appl. Mater. Interfaces* **2019**, *11*, 41157−41164.
(41) Chang, Y. Y.; Wu, Z. Y.; Sun, Q. X.; Zhuo, Y.; Chai, Y. Q.; Yuan, R. *Anal. Chem.* **2019**, *91*, 8123−8128.
(42) Lu, S. S.; Wang, S.; Zhao, J. H.; Sun, J.; Yang, X. R. *Anal. Chem.* **2019**, *91*, 1452−1459.